Boundary-Layer Meteorology (2020) 175:397–416
https://doi.org/10.1007/s10546-020-00512-1

RESEARCH ARTICLE

High-Resolution Estimation and Spatial Interpolation of Temperature Structure in the Atmospheric Boundary Layer Using a Small Unmanned Aircraft System

Benjamin L. Hemingway[1] · Amy E. Frazier[2] · Brian R. Elbing[3] · Jamey D. Jacob[3]

Received: 24 May 2019 / Accepted: 11 March 2020 / Published online: 6 April 2020

Abstract
Knowledge of the effects of small-scale fluctuations in temperature on light transmission in the atmosphere is necessary for the calibration of remote sensing instruments as well as for the understanding of turbulent heat transport in the atmospheric boundary layer. Recent developments in small unmanned aircraft systems (sUAS) have allowed for direct, spatial in situ estimation of temperature in the ABL at very high temporal and spatial resolutions. Structure functions are estimated from vertical profiles of temperature collected using an ultrasonic anemometer mounted on an sUAS. Using geostatistical methodologies specifically developed for spatially non-stationary and spatially dependent random variables, we estimate temperature structure from six profiles reaching roughly 500 m in altitude A mean function is specified to account for the variation in temperature with altitude and the structure function is estimated from the residuals. A 2/3 scaling exponent is fitted to the resulting curves commensurate with the inertial subrange of turbulence. The resulting structure functions of residuals are able to resolve the inertial subrange on most profiles at a range of separation distances. We find that geostatistical methods for spatially non-stationary random variables are well suited in certain cases to describing the vertical structure of temperature in the boundary layer.

Keywords Drones · Fluid mechanics · Kriging · Remotely-piloted vehicle · Variogram

1 Introduction

Small-scale fluctuations in temperature are of considerable importance in meteorology. Practically, their effects on sound and light propagation in the atmosphere allow for their use in

✉ Benjamin L. Hemingway
ben.hemingway@okstate.edu

[1] Department of Geography, Oklahoma State University, Oklahoma 74078, USA

[2] School of Geographical Sciences and Urban Planning, Arizona State University, Arizona 85281, USA

[3] Department of Mechanical and Aerospace Engineering, Oklahoma State University, Oklahoma 74078, USA

the calibration of remote sensing instruments (Wainwright et al. 2015). Theoretically, the small-scale turbulent motions that cause these fluctuations are most likely to be universal, leading to a better understanding of turbulence at all scales (Sreenivasan and Antonia 1997). Small-scale fluctuations of temperature have been theorized to be analogous to velocity fluctuations, which led Obukhov (1949) to characterize small-scale temperature fluctuations in the context of Kolmogorov similarity theory. Kolmogorov (1941a) proposed that in the inertial subrange, where the flow statistics are dependent only on the energy dissipation rate, eddies contained therein are homogenous (spatially stationary), isotropic, and independent of the larger, energy-containing eddies. In accordance with Kolmogorov's theory in the inertial subrange, temperature increments represented by $T(\boldsymbol{x}+h)-T(\boldsymbol{x})=\Delta T$, where T is the temperature measured at location $\boldsymbol{x}$, and h is a spatial separation distance, should scale as

$$\Delta T(h)^p = C_p h^{\frac{p}{3}}, \tag{1}$$

where p is the moment of temperature increments, and C_p is a proportionality factor. When $p=2$, the square of the temperature increments, $\Delta T(h)^2$, is the second-order structure function, and C_2 is known in micrometeorology as the temperature structure function parameter or more commonly the temperature structure parameter, C_{T}^2. The value of p in Eq. 1 need not be an integer (Mathieu and Scott 2000), and evidence suggests that flows in the atmospheric boundary layer (ABL) deviate from this scaling relationship, a phenomenon known as intermittency (Monin and Yaglom 1975). Kolmogorov (1941a) proposed that the energy dissipation rate remains constant, leading to a linear similarity relationship between the scaling exponent $p/3$ and the structure function of order p. However, the large energy-containing eddies, which provide the statistical input to the small-scale energy cascade, are thought to vary in intensity, causing random fluctuations in temperature and velocity increments to propagate down through the energy cascade (Mathieu and Scott 2000). This propagation leads to a breakdown of the theorized similarity relationship, particularly at higher-order moments. It has been suggested that the structure function of temperature is more sensitive to intermittency than the structure function of velocity (Antonia et al. 1984), although Gawedski and Kupainien (1995) demonstrated that the scaling relationships in Eq. 1 hold when $p=2$ for temperature measurements.

The structure functions and inertial subrange scaling relationships of temperature have been studied empirically in both the laboratory environment (Cioni et al. 1995) as well as in the ABL (Vindel et al. 2008). However, most data collection occurs in the time domain, and measurements are converted to the spatial dimension through the application of the Taylor (1938) frozen turbulence hypothesis, which is a key assumption in assessing the validity of the scaling relationships (Grossman and Lohse 1994). Capturing a spatial snapshot of conditions in the ABL has remained challenging. Recent technological advancements have led to the adoption of small unmanned aircraft systems (sUAS) in the atmospheric sciences, as they provide the capability for collecting data to compute inherently spatial, two-point correlation statistics (Jacob et al. 2018).

The use of sUAS for atmospheric sampling is not entirely new, however, and goes back to at least the 1960s (Smith 2011). Konrad et al. (1970) proposed using small, remotely-controlled aircraft for collecting temperature and humidity data near the ground. More recent advancements in sUAS technology have led to their use in a variety of meteorological sensing applications, such as high-resolution distributed temperature sensing of the morning ABL transition (Higgins et al. 2018) and pre-convective environments (Koch et al. 2018), obtaining vertical profiles of wind velocity for cloud-aerosol interactions (Calmer et al. 2018), and estimating the sensible heat flux (Lee et al. 2017). A handful of studies have estimated the temperature structure function (and correspondingly C_2) using sUAS in the ABL (van

den Kroonenberg et al. 2012; Bonin et al. 2015; Wainwright et al. 2015; Braam et al. 2016; Platis et al. 2017) and were able to resolve the inertial subrange through the theorized scaling relationship (Eq. 1). However, these studies compiled estimates of C_2 collected at discrete altitudes using horizontal transects across heterogeneous terrain (van den Kroonenberg 2012) or spiral ascents, estimating C_2 horizontally at discrete attitudes and constructing a C_2 profile (e.g., Bonin et al. 2015; Wainwright et al. 2015). Horizontal estimates of the temperature structure may be subject to influences of surface heterogeneity, making it difficult to distinguish the surface influences on the statistics of the turbulence (van den Kroonenberg et al. 2012; Platis et al. 2017). The constant C_2 has been estimated from continuous vertical sUAS profiles by Platis et al. (2016).

The question becomes whether the estimation of C_2 from continuous profiles is necessary and appropriate. Isotropic turbulence, within which C_2 estimates are valid, is inherently three-dimensional. For example, it has been suggested that coherent structures in the ABL are oriented obliquely at angles up to 45 degrees from the surface (Marusic and Heuer 2007). Additionally, the impacts of shear and buoyancy on the transport of heat and momentum in the ABL are predominately observed in the vertical direction. Practically speaking, the structure function is the key component to the spatial interpolation methodology known as kriging (or Gaussian process regression). Most natural variability, such as that of temperature, exhibits some degree of spatial autocorrelation, that is, measured values nearer to each other are more similar to each other than those measured at greater distances. The structure function (or variogram) is a measure of spatial autocorrelation. For these reasons, estimating C_2 from continuous vertical profiles has value not only for understanding the physical process, but also for representing it statistically.

Given the need for investigating temperature structure using vertical profiles, there are challenges to overcome. First-order differences may be stationary at short separation distances; however, the structure function estimated using data spanning greater vertical separation distances are, by nature, spatially non-stationary, and thus a modified form of the structure function must be used to account for the non-constant mean across the vertical spatial domain. Geostatistics is a branch of spatial statistics focusing on predicting probability distributions of spatial and spatio-temporal datasets. Geostatistics is widely used in the Earth sciences, including geography and geology, to predict values of parameters between sampled data points. Geostatistical approaches are well suited for random variables due to the ability to accommodate the spatial non-stationarity and spatial dependence inherent to such data. Kolmogorov (1941b) proposed the structure function to assign weights for the optimal prediction of turbulent quantities. Conceptually, similar techniques were simultaneously developed by others in a variety of disciplines (see Cressie 1990 for a thorough history), but the theory of geostatistics was coalesced by Matheron (1963). This theoretical foundation serves as the basis for using geostatistical analysis for atmospheric research, which underpins the present study.

The main objective is to characterize the spatial structure of vertical temperature observations through profiles captured via sUAS using geostatistical tools. To this end, we pursue three sub-objectives:

1. Capture the structure of the temperature field in the vertical dimension using the variogram to identify sample separation distances that are inherent to the inertial subrange of turbulence by assessing ranges of separation distances that follow a 2/3-power law model.

2. Assess the degree of deviation from the theorized second-order scaling relationships through cross validation of universal kriging, a distance-weighted method of interpolation that will use the 2/3-power law model for assignment of weights.
3. Determine specific portions of the continuous, vertical profile for which the 2/3-power law model best fits the data through assessment of prediction residuals at each estimated point.

2 Theory

For a continuous variable such as temperature, at any given point, $\boldsymbol{x}$, there is not a single value, but one of any number of potential temperature values. The realization of a single value is a random variable $Z(\boldsymbol{x})$, having a mean, standard deviation, and probability density function. A random variable for all locations in $\boldsymbol{x} = (\boldsymbol{x_1}, \boldsymbol{x_2} \ldots \boldsymbol{x_n})$ becomes the random function used to describe the random variable. An actual realization of the random process is known as a regionalized variable (Webster and Oliver 2007), which is made up of three parts: (1) a structural component (with a constant mean or a trend), and a random component made up of, (2) spatially correlated variation, and (3) uncorrelated noise. The random model can be written as

$$Z(\boldsymbol{x}) = \mu + \varepsilon'(\boldsymbol{x}) + \varepsilon'', \tag{2}$$

where $Z(\mathbf{x})$ is the random variable, μ is the mean, $\varepsilon'(\mathbf{x})$ is a spatially-autocorrelated error component, and ε'' is a random component with a mean of zero. Here, $\varepsilon'(\boldsymbol{x})$ has a covariance $C(\boldsymbol{h}) = E\left[\varepsilon'(\boldsymbol{x})\varepsilon'(\boldsymbol{x}+h)\right]$) that depends only on h, the spatial separation distance between sample points (Webster and Oliver 2007). Note that the covariance exists and depends only on h, an assumption known as second-order stationarity. A random function, however, may not meet this assumption, in which case the mean and covariance are undefined (Myers 1989). An alternative and less restrictive form of stationarity can then be used, known as the intrinsic hypothesis,

$$E[Z(\boldsymbol{x}) - Z(\boldsymbol{x}+h)] = 0, \tag{3}$$

where the expected first difference between $Z(\boldsymbol{x})$ and itself at separation distance h is zero. The variance of the difference is used instead of the covariance,

$$var[Z(\boldsymbol{x}) - Z(\boldsymbol{x}+h)] = 2\gamma(h), \tag{4}$$

where γ is the variance (also called the semivariance), and $2\gamma(h)$ is the variogram (Cressie 1993).

If the expectation of $Z(\boldsymbol{x})$ does not only depend on separation distance h, but also on position $\boldsymbol{x}$, the random variable is not spatially stationary. In this case, the deterministic structural component must be separated from the random component (the spatially-autocorrelated variation and white noise). This is accomplished through specification of a mean function in the random model,

$$Z(\boldsymbol{x}) = \mu(\boldsymbol{x}) + \varepsilon'(x) + \varepsilon'', \tag{5}$$

where $\mu(\boldsymbol{x})$ is a deterministic mean function. The typical approach for specifying a mean function is a simple linear regression of variable Z and the spatial coordinate(s). The variogram is then calculated from the residuals,

$$2\gamma(h) = E\left[\{\varepsilon'(\boldsymbol{x}) - \varepsilon'(\boldsymbol{x}+h)\}^2\right]. \tag{6}$$

The variogram, in addition to describing the spatial continuity of a random variable, is also used during interpolation to assign spatial weights in order to achieve the best linear unbiased predictor (BLUP) for a random variable Z at an unsampled point x_0. Computing the variogram allows for the weighting of sampled observations based on their distance from the unsampled point. The variogram exploits the spatial autocorrelation inherent to the data; points nearer the origin are weighted greater than the more distant points. Since temperature differences are theorized to obey a power-law relation to their separation distance, weighted interpolation provides a means of assessing the portions of the profile that most likely obey the theorized scaling relationship.

Finding the value of Z at x_0 (i.e., interpolation) is accomplished through a procedure known as universal kriging, and BLUP is achieved through a weighted linear sum,

$$\hat{Z}\boldsymbol{x}_{(0)} = \sum_{i=1}^{N} \lambda_i f_k(\boldsymbol{x}_i), \tag{7}$$

where λ_i are spatial weights, and f_k are functions of the spatial coordinates. For a one-dimensional dataset, such as the vertical profiles in this study, there are $k = 2$ covariates where $f_1 = 1$ and $f_2 = x_1$. As a condition of the unbiasedness, the weights sum to 1, $\sum_{i=1}^{N} \lambda_1 = 1$. Weights are solved, in matrix notation, as

$$\boldsymbol{A}\boldsymbol{\lambda} = \mathbf{b}, \tag{8}$$

where $\boldsymbol{A}$ is a symmetrical $(N + k) \times (N + k)$ matrix of the γ values of the residuals between all sampled points and the spatial coordinate covariates, $\mathbf{b}$ is a vector of γ values of the residuals between all sampled points and the unsampled point and the corresponding spatial covariates, and $\boldsymbol{\lambda}$ is a vector of weights and Lagrange multipliers used for optimization, which expands to

$$\begin{bmatrix} \gamma_{11} & \cdots & \gamma_{1n} & f_{11} & \cdots & f_{1k} \\ \vdots & \ddots & \vdots & \vdots & \ddots & \vdots \\ \gamma_{n1} & \cdots & \gamma_{nn} & f_{n1} & \cdots & f_{nk} \\ f_{11} & \cdots & f_{1n} & 0 & \cdots & 0 \\ \vdots & \ddots & \vdots & \vdots & \ddots & 0 \\ f_{k1} & \cdots & f_{kn} & 0 & \cdots & 0 \end{bmatrix} \times \begin{bmatrix} \lambda_1 \\ \vdots \\ \lambda_n \\ \psi_1 \\ \vdots \\ \psi_k \end{bmatrix} = \begin{bmatrix} \gamma_{10} \\ \vdots \\ \gamma_{n0} \\ f_{10} \\ \vdots \\ f_{k0} \end{bmatrix}, \tag{9}$$

where the Lagrange multipliers are denoted by ψ (Webster and Oliver 2007). The BLUP is found through minimization of the kriging variance

$$\sigma_k^2 = 2 \sum_{i=1}^{N} \lambda_i \gamma(\boldsymbol{x}_0 - \boldsymbol{x}_i) - \sum_{i=1}^{N} \sum_{j=1}^{N} \lambda_i \lambda_j \gamma\left(\boldsymbol{x}_i - \boldsymbol{x}_j\right). \tag{10}$$

3 Materials and Methods

3.1 Study Area

The data for this study were collected on 18 July 2018 in the San Luis Valley of Colorado during the Lower Atmospheric Process Studies at Elevation - a Remotely-piloted Aircraft Team Experiment (LAPSE-RATE) field campaign as part of the International Society of Atmospheric Research using Remotely-piloted Aircraft (ISARRA) annual meeting. LAPSE-RATE

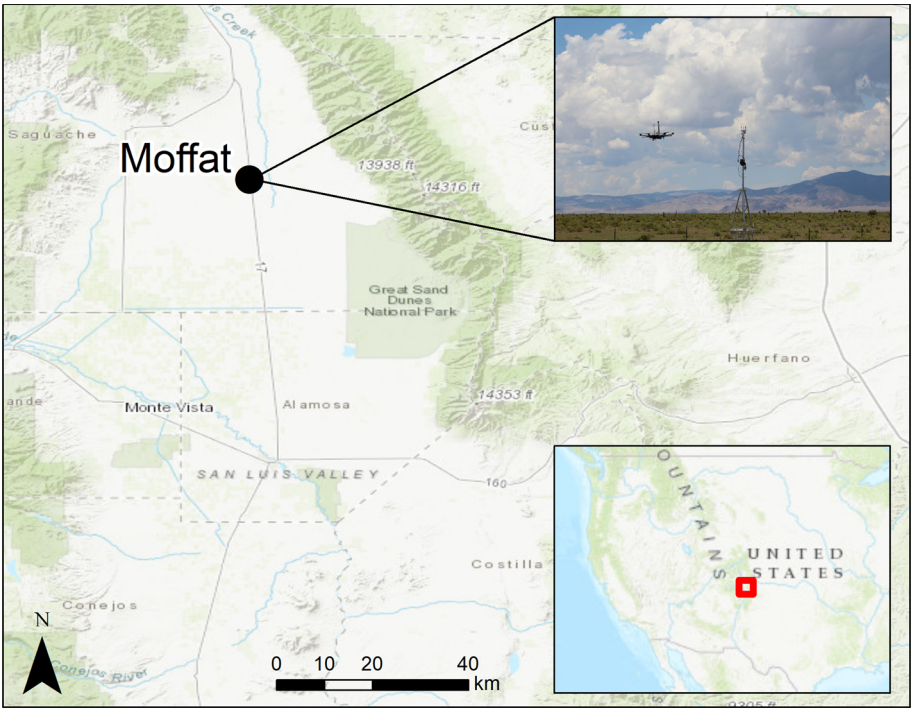

Fig. 1 Map of the Moffat flight location in the San Luis Valley (Base map: Esri)

was a coordinated effort that included more than 100 participants from 13 institutions and organizations. During the six-day campaign, more than 35 unmanned aircraft were deployed and completed 1,287 flights, accumulating more than 260 flight hours to capture data for a variety of scientific objectives, including observations of the morning boundary-layer transition, the diurnal cycle of valley flows, convective initiation, and aerosol properties, among others (Barbieri et al. 2019).

Geographically, the San Luis Valley is a high-desert valley located in south-central Colorado, with an average elevation of approximately 2,300 m above mean sea level (m.s.l.) The valley is flanked by mountain peaks exceeding 4300 m m.s.l. and frequently experiences convective storms during late afternoons in the summer. While flight activities for the comprehensive LAPSE-RATE campaign spanned six days and occurred at multiple locations across the valley, the data used in this study were captured at one location, Moffat, a rural area 30 km north-east of Alamosa, Colorado, at an elevation of 2,310 m m.s.l. While flights occurred on the grounds of a school, the vegetation immediately adjacent was dominated by deciduous shrubs (Fig. 1).

Flights consisted of six vertical profiles captured during the early morning and continuing through the mid-day boundary-layer transition (Table 1). All flights were conducted under a certificate of authorization issued by the Federal Aviation Administration (FAA), which allowed maximum altitude to exceed the federally-mandated maximum of 123 m (400 ft.). Maximum altitudes on 18 July ranged from 490.0 to 499.7 m above ground level (a.g.l.). Ascent speeds averaged 3.3 m s^{-1}.

Table 1 Flight times and maximum altitudes for the 12 profiles. All times are local (UTC-6 h)

Flight #	Start time	End time	Max alt a.g.l. [m]
1	0708:02	0710:48	490.9
2	0759:41	0802:42	499.2
3	0859:43	0902:45	499.2
4	1059:56	1101:48	499.7
5	1146:50	1149:47	498.2
6	1229:02	1301:02	499.1

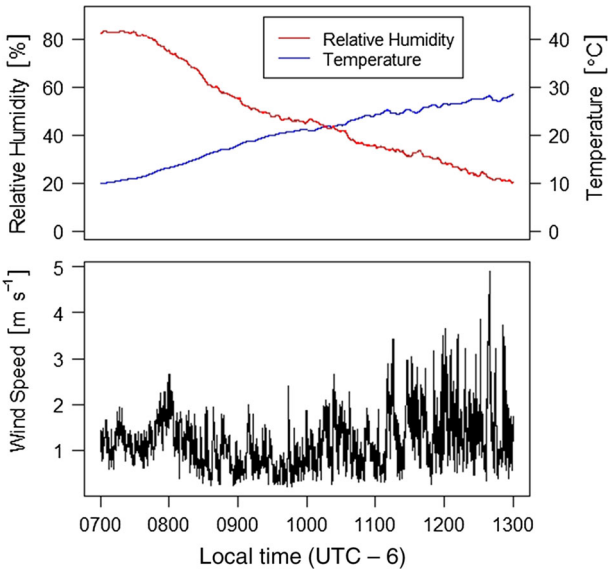

Fig. 2 Surface weather conditions at the Moffat flight location, measured approximately 3 m a.g.l

3.2 Surface Weather Conditions at the Study Location

Surface weather conditions at the Moffatt site were recorded from a meteorological tower approximately 3 m in height (Fig. 2). Temperature, relative humidity, pressure, and wind speed and direction (not shown) were recorded throughout the duration of flight activities. The temperature at the surface ranged from approximately 10° C at 0700 local time (LT, UTC-6 h) to nearly 30° C by 1300 LT. Relative humidity decreased from 80% at 0700 LT to roughly 10% by 1300 LT. Wind speeds were low in the morning at roughly 1 m s^{-1}, increasing to 5 m s^{-1} by the early afternoon.

3.3 Radiosonde Measurements

In addition to the surface weather observations, radiosondes were deployed several times throughout the day. Profiles of potential temperature and wind speed captured at three different times throughout the flight activities show a slight inversion during the 0830 LT radiosonde above approximately 200 m a.g.l. The 1001 LT radiosonde profile shows a slight inversion at around 500 m, and the 1131 LT profile indicates a mixed boundary layer (Fig. 3).

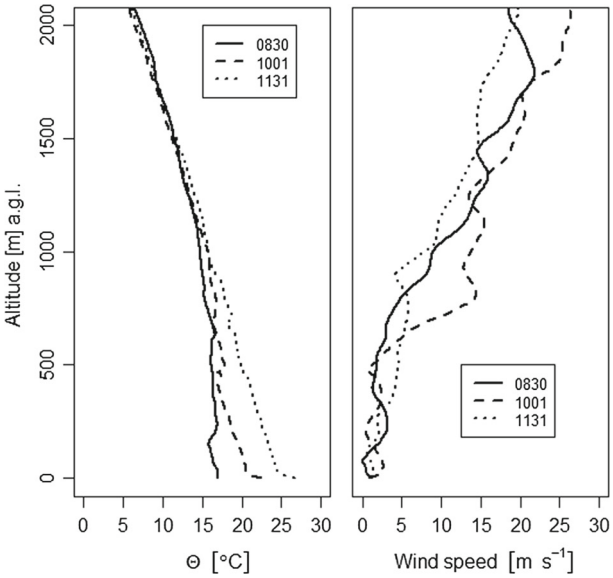

Fig. 3 Radiosonde potential temperature [Θ] and wind-speed profiles

3.4 Aircraft and Instrumentation

The aircraft platform was a DJI Matrice 600 (DJI Shenzhen, Guangdong, China), which is a hexacopter measuring 1.13 m in diameter and weighing 9.1 kg. The platform has a 7-kg payload capacity and is therefore capable of accommodating larger meteorological instruments. The Matrice 600 was outfitted with a Young Model 81000 (R. M. Young Company, Traverse City, MI) ultrasonic anemometer weighing 1.2 kg, which was affixed to the aircraft using custom designed mounts (Fig. 4). Vehicle telemetry and atmospheric observations were synchronized and logged at 32 Hz onto a Stabilis flight control module developed at Oklahoma State University (Donnell et al. 2018). The resulting aggregate is referred to as a WxUAS.

The placement of the anemometer centrally on the aircraft and above the propellers (Fig. 4) minimizes effects of rotor downwash, although contamination may occur during high descent rates due to rotor downwash and separation over the WxUAS fuselage (Avery et al. 2019), which limits data collection to during hover and ascent flight modes. Consequently, only data collected during the ascent were analyzed in an effort to ensure temporal stationarity and limit interference from the aircraft. The anemometer was validated, while flying on the platform, against the Mobile UAS Research Collaboratory (MURC), which is a ground-based system operated by the University of Colorado–Boulder's Integrated Remote and In-Situ Sensing (IRISS) program that provides instrumentation for reference comparisons. The MURC system has a 15-m extendable mast hosting a suite of meteorological sensors. The Young 81000 mounted on the WxUAS compared well against the MURC measurements while flying at 15 m for a sustained period of 8 min (Barbieri et al. 2019).

Fig. 4 DJI Matrice 600 hexacopter outfitted with a Young Model 81000 ultrasonic anemometer on top (Photo: Jamey Jacob)

3.5 Calculation of Sonic Temperature

We utilized temperature measurements captured with the Young Model 81000 ultrasonic anemometer. Sonic temperature can be determined through the calculation of the speed of sound, which is done through the transit time method (Brock and Richardson 2001). An acoustic pulse is emitted in opposing directions between two transducers, and the speed of sound can be determined through

$$c = \frac{d}{2}\left(\frac{1}{t_1} - \frac{1}{t_2}\right), \tag{11}$$

where c is the speed of sound, t_1 and t_2 are the transit times of the acoustic pulse between opposing transducers, respectively, and d is the distance between the transducers. Sonic temperature can then be computed directly using the speed of sound

$$T = c^2 k R, \tag{12}$$

where T is sonic temperature, k is the ratio of specific heat of air, and R is the specific gas constant. When water vapour pressure is low compared to the atmospheric pressure, sonic temperature becomes a good approximation to the actual air temperature. In typical conditions, errors are less than 1% (Harrison 2015).

On a three-axis sonic anemometer, such as the Young 81000, sonic temperature is computed using the vertical velocity component, w The speed of sound calculation is independent of wind speed in the direction parallel to the acoustic pulse. Consequently, the vertical motion of the aircraft should have negligible effects on the calculation of the speed of sound and thus sonic temperature.

In previous studies, good agreement has been obtained between temperature measurements from sonic anemometers and fast-response hot-wires, demonstrating the applicability of this technique (Schotanus et al. 1983). In addition, observed values of C_2 from an sUAS compared well with other measurements (in this case, sodar), but differed from numerical predictions, potentially due to site-specific characteristics such as topography (Wainwright et al. 2015). In previous studies (Van den Kroonenberg et al. 2012; Braam et al. 2016) the horizontal profiles

of temperature obtained from the sUAS were treated as a time series and converted to the spatial domain through the application of Taylor's hypothesis and the mean ground speed or the true air speed. Profiles in the present study were treated as a true spatial series.

Estimates of C_2 are sensitive to the time constant of the temperature sensor, that is, the time it takes the sensor to respond to a new temperature value. A sensor time constant smooths the data and can result in lowering C_2 estimates by as much as 5% (Platis et al. 2016). Wainwright et al. (2015) applied a correction to account for the sensor time constant. In contrast, sonic temperature used here in has no appreciable time delay in adjusting to the speed of sound and thus sonic temperature. The time constant is effectively the sampling rate, which was 32 Hz.

3.6 Estimating Sample Variograms

Sample variograms $2\hat{\gamma}(h)$ were estimated from the temperature profiles using the method-of-moments estimator,

$$2\hat{\gamma}(h) = \frac{1}{N(h)} \sum_{i=1}^{N(h)} \{Z(\boldsymbol{x_i}) - Z(\boldsymbol{x_i} + h)\}^2, \tag{13}$$

where $Z(\boldsymbol{x_i})$ is the observed value at location $\boldsymbol{x_i}$ and $Z(\boldsymbol{x_i} + h)$ is the observed value at location $\boldsymbol{x_i}$ separated by distance h. N is the number of sample pairs at each separation distance (Cressie 1993). The variogram estimator (Eq. 13) was applied to the residuals of the mean function as specified in Sect. 2. Residuals were discretized into bins based on their spatial separation distance from one another. A bin width of 1 m was selected as a compromise between variogram clarity and the ability to capture the variable structure. Bins were set every 1 m up to 100-m separation distances.

3.7 Fitting Model Variograms

Sample variogram data are typically modelled to mitigate the influence of noise and scatter (Webster and Oliver 2007). The power model variogram is defined as

$$2\gamma(h) = C_0 + C_2 h^{\alpha}, \tag{14}$$

where α is a scaling exponent, and C_0 is an error component known as the nugget effect. In many cases, the variogram may intersect the y axis at a point greater than zero. This is attributed to micro-structure of the data smaller than that of the sampling distance, measurement error, or spatial positioning errors (Chiles and Delfiner 2012). The power model variogram is only valid when $0 > \alpha > 2$ (Webster and Oliver 2007), where a value of $\alpha = 1$ would result in a linear variogram. Power model variograms were fit to the sample variograms using weighted non-linear least squares with $\alpha = 2/3$ following the theory of Kolmogorov (1941a). The weights are given by $N(h)/2\gamma(h)^2$, where N is the number of point-pairs in the sample variogram estimate, which allows greater weight to be given to sample variogram point-pairs nearer the origin.

3.8 Universal Kriging and Quantitative Assessment of Model Fit

While comparisons between the sample and modelled variograms can indicate the separation distances at which the inertial subrange can be resolved using the theorized scaling relationship, they do not allow for a localized determination of how the modelled variogram fits the

data. To quantitatively assess model fit, we used universal kriging to estimate values across the profile and then cross-validated those estimates against the modelled values. Due to the very high density of the data points (32 Hz), a stratified random sample of observations was selected such that there was at least one observation selected per metre in altitude across the entirety of the profiles. Universal kriging was then performed using the fitted 2/3-power law model variogram for weight assignment as described in Sect. 2.

Model fit was assessed through the cross-validation of the universal kriging estimates. A leave-one-out, cross-validation procedure was implemented such that each observation was iteratively excluded from the sample, and its temperature value was predicted using the remaining observations. This process was repeated until temperature estimates for all observations were obtained. The statistic used to measure the goodness of the model variograms was the mean square deviation ratio

$$MSDR = \frac{1}{N} \sum_{i=1}^{N} \frac{\left\{ Z(\boldsymbol{x}_i) - \hat{Z}(\boldsymbol{x}_0) \right\}^2}{\sigma^2(\boldsymbol{x}_i)}, \tag{15}$$

where $Z(\boldsymbol{x}_i)$ is the measured temperature value, $\hat{Z}\boldsymbol{x}_{(0)}$ is the temperature estimate, and $\hat{\sigma}^2(\boldsymbol{x}_i)$ is the estimated kriging variance. If the model variogram fits the data well, the kriging variance and the squared residual of the estimate will be close in value, resulting in $MSDR \approx 1$ (Webster and Oliver 2007). A profile of the *SDR* value at every prediction location provides a localized assessment of model fit. Analysis was completed using the gstat package (Pebesma 2004) in the R-statistical computing language.

4 Results

4.1 Profiles

Temperature profiles (Fig. 5) show the progression of the ABL throughout the morning transition. The first two profiles exhibit an increase in temperature with altitude suggesting the remnants of a stable nocturnal boundary layer. The four subsequent profiles, occurring from 0859–1259 LT, are indicative of the boundary-layer transition to a mixed state as the morning progressed into the early afternoon. The two middle WxUAS profiles, 0859 LT and 1059 LT, display very little variability about their mean compared to the others. The penultimate WxUAS profile displays a slight increase in temperature between 10 and 40 m a.g.l. as well as a relative increase in temperature between 100 m and 200 m a.g.l. This increase in temperature begins sharply and may be an artefact of the sensor. Similarly, the final WxUAS profile depicts a similar segment with an increase in temperature between approximately 30 and 80 m a.g.l.

The radiosonde profiles of temperature (Fig. 5, black lines) display relative agreement with the sonic temperature profiles captured with the WxUAS. The profile of the 0830 LT radiosonde depicts the same increase in temperature with altitude at roughly 200 m a.g.l. as the 0708 LT and 0759 LT WxUAS profiles. The 1001 LT radiosonde profile shows a smooth decrease in temperature with altitude, similar to the 0859 LT and 1059 LT WxUAS profiles. The 1131 LT profile also shows a smooth decrease in temperature with altitude, unlike the nearly contemporaneous 1146 LT WxUAS profile, which shows greater variability about the mean. This difference is likely a result of the low resolution of the radiosonde data having a smoothing effect.

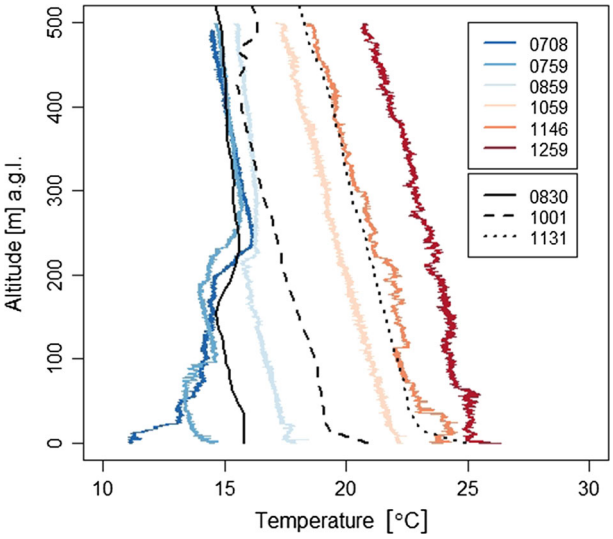

Fig. 5 Temperature profiles captured by sUAS (coloured lines) and radiosondes (black lines). Radiosonde profiles are not displayed as potential temperature, but in temperature for comparison to the sonic temperature profiles captured by the WxUAS. All times are local (UTC-6 h)

4.2 Variograms

Variograms estimated from data from the six WxUAS profiles (Fig. 6) reveal a variety of structural characteristics. Recall that in the inertial subrange, the sample variogram should closely follow the 2/3-power law model variogram (Eq. 14). The model variogram, which has been forced to follow 2/3 power, is represented with the solid red line; sample variograms are represented by the black circles (Fig. 6).

To identify the sample separation distances that are inherent to the inertial subrange of turbulence and assess the degree of deviation from the theoretical 2/3-power law scaling relationship, we visually assessed the sample variogram fits and also quantitatively measured fit via the *MSDR* values between the sample and modelled variograms. The 2/3-power law model variograms do not fit the first three profiles well (Fig. 6a–c). The sample variograms increase as a function of distance at a greater rate than that of the model variogram for Flights 1–3. The C_2 and C_0 estimates are reported in Table 2 but are not meaningful considering the data do not fit the model. The *MSDR* values are therefore not reported for these three flights. The 2/3-power law model variograms fit profiles from Flights 4–5 well, as the sample variogram follows the model variogram closely throughout the 100 m range of separation distances (Fig. 6d, e). A nugget effect, C_0, was estimated on these two models, with values of 0.014 K^2 for both. C_2 estimates for Flights 4–5 were 0.001 K^2 $m^{-2/3}$ and 0.010 K^2 $m^{-2/3}$, respectively. Flight 4 had $MSDR = 0.993$, meaning the 2/3-power law model fit the data quite well, whereas Flight 5 had $MSDR = 0.53$, indicating a moderate fits. The model variogram fit the final profile, Flight 6, well up to roughly the 50-m separation distance, but then the sample variogram begians to decrease with distance until the maximum separation distance of 100 m is reached (Fig. 6f). The C_2 estimate for Flight 6 decreased from the previous flight to 0.006 K^2 $m^{-2/3}$. A C_0 value of 0.022 K^2 was estimated for Flight 6, and $MSDR = 0.677$ (Table 2).

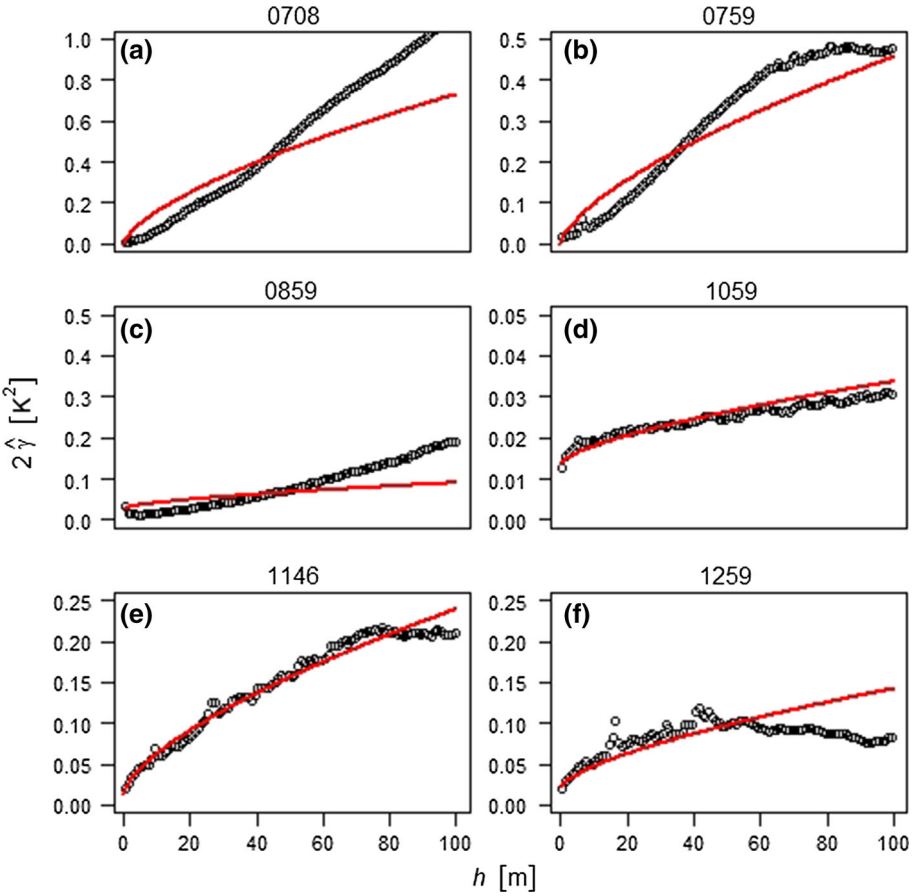

Fig. 6 Sample variograms (circles) and fitted 2/3-power law model variograms (red lines) for all full profiles (h is vertical separation distance between sample pairs, and $2\hat{\gamma}$ is the variogram)

Table 2 Variogram parameter estimates and fit diagnostic for Flights 1–6

Flight #	C_2	C_0	α	*MSDR*
1	0.034	0.000	2/3	–
2	0.021	0.000	2/3	–
3	0.003	0.027	2/3	–
4	0.001	0.014	2/3	0.993
5	0.010	0.014	2/3	0.539
6	0.006	0.022	2/3	0.677

Computing the structure function across the full extent of Flights 1–3 is likely not appropriate given the slight inversion in the profiles at roughly 250 m a.g.l. To account for this inversion, the variogram and its parameters were estimated for Flights 1–3 from the data below 250 m a.g.l. and above 250 m a.g.l. separately, and the results are presented in Fig. 7 and Table 3.

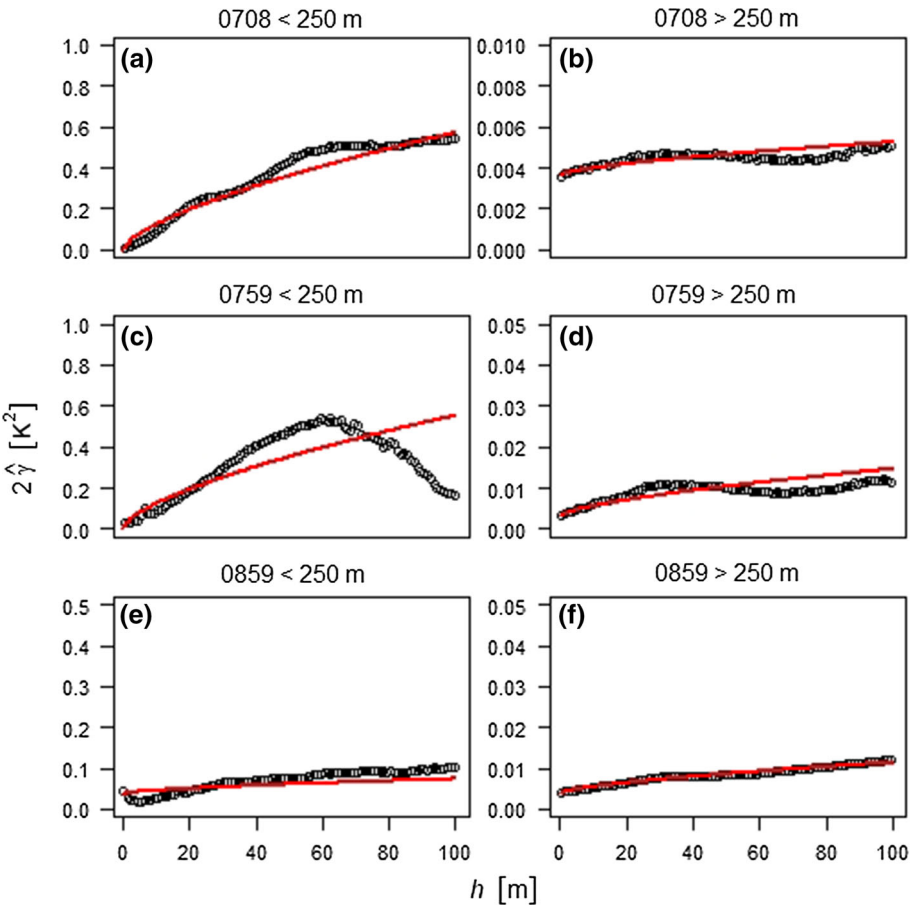

Fig. 7 Sample variograms (points) and fitted 2/3-power law model variograms (lines) for 0708, 0759, and 0859 profiles for altitudes above and below 250 m a.g.l. (h is vertical separation distance between sample pairs, and $2\hat{\gamma}$ is the variogram)

Table 3 Variogram parameter estimates and fit diagnostic for Flights 1–3 below 250 m a.g.l. (a) and above 250 m a.g.l. (b)

Flight #	C_2	C_0	α	*MSDR*
1a	0.027	0.000	2/3	0.309
1b	0.000	0.004	2/3	1.067
2a	0.025	0.007	2/3	1.086
2b	0.001	0.003	2/3	1.086
3a	0.002	0.038	2/3	0.286
3b	0.000	0.004	2/3	0.858

Variograms estimated from the lowest 250 m a.g.l. from the first three profiles display very different structural behaviour than the variograms estimated from 250 m a.g.l. and above. The variogram estimated from Flight 1a roughly follows the 2/3- power law model variogram with a slight deviation between 40- and 80-m separation distances (Fig. 7a). C_2 was estimated to be 0.027 K^2 m $^{-2/3}$, and a C_0 value was not fit. The *MSDR* value was estimated to be

0.309. The variogram for Flight 2a increases at a rate greater than the 2/3-power law model variogram (Fig. 7c). The variogram peaked at a separation distance of about 60 m, and then the variogram began to decrease. The variogram of Flight 3a roughly follows the 2/3-power law model (Fig. 7e), but the C_2 value was estimated to be 0.002 K^2 m $^{-2/3}$, nearly one-tenth the value of C_2 estimated from Flights 1a and 2a. A C_0 value was estimated to be 0.038 K^2, and the *MSDR* value was estimated to be 0.286, suggesting the model was poorly fit. The variograms for Flights 1b, 2b, and 3b all appear similarly flat (Fig. 7b, 7d, 7f) and had similar estimates of C_0. Flight 1b had a C_2 estimate near zero, while flights 2b and 3b had C_2 estimates of 0.001 and 0.002 K^2 $m^{-2/3}$, respectively.

4.3 Cross-Validation of Kriging Estimates

To distinguish specific altitudes for which the scaling relationship is valid, we assessed the universal kriging estimates of the temperature profiles using weights assigned by the 2/3-power model variogram. As a localized measure of how well the 2/3-power law variogram fit the data, the *SDR* value was estimated at every metre along the profiles using the method described in Sect. 3.8. As with the *MSDR* statistic, local *SDR* estimates near 1 indicate the model variogram fit the data well, meaning that the inertial subrange at that location was well resolved through theorized scaling. Flights 1–3 were analyzed in the sections above and below 250 m a.g.l. separately, using the variogram parameters listed in Table 3. The *SDR* estimates from Flights 1a, 2a, and 3a are less than 1 throughout the extent of the 250 m subset of the profile (Fig. 8). The *SDR* value estimated from Flight 1b oscillates, crossing 1 several times along the extent of the profile subset. Flight 2b *SDR* estimates hover near 1 between 300 and 400 m a.g.l. and then remain below 1 throughout the extent of the profile. Flight 3b *SDR* estimates display a similar pattern to those of 2b, having values near 1 in the portion of the profile near 300 m a.g.l. and dropping below 1 as the profile approaches its maximum extent near 500 m a.g.l.

Recall that Flight 4 had the best *MSDR* value of 0.993. This fit is similarly reflected in the local *SDR* estimates along the profile. The smoothing spline closely follows a value of 1, with slight deviations near 150 m and 350 m a.g.l. Flight 5, with an *MSDR* of 0.539, displays local *SDR* estimates of less than 1 throughout the extent of the profile, with the exception of the lowest 50 m a.g.l. Flight 6, with $MSDR = 0.677$, is slightly more representative of the 2/3-power law model variogram than Flight 5. Local *SDR* estimates roughly follow a value of one until 300 m a.g.l., where they dip below 1 for the remainder of the profile.

In summary, the 2/3-power model variogram fit Flights 4–5 well across the entire range of separation distances. The model fit Flight 6 well for a large portion of the separation distances, up to 50 m (Fig. 6). For Flights 1–3, the presence of an inversion forced the need to separate the measurements into two groups: below 250 m a.g.l. and above 250 m a.g.l. After this was done, the 2/3-power law model variogram visually appeared to fit the sample variogram well in Flight 1a and 3a (Fig. 7a, e), but when fit was measured quantitatively through the squared deviation ratio, the result indicated these flights were poorly fit, resulting in poor estimates. The variogram of Flight 2a appeared to have a wave-like nature (Fig. 7c), indicative of periodicity in the data. Results from this portion of the analysis suggest that the 2/3-model variogram fit to the residual process of a temperature profile can be used to identify sample separation distances inherent to the inertial subrange in well-mixed conditions. However, the model was less successful in resolving the inertial subrange in the early morning flights, particularly below the slight temperature inversion.

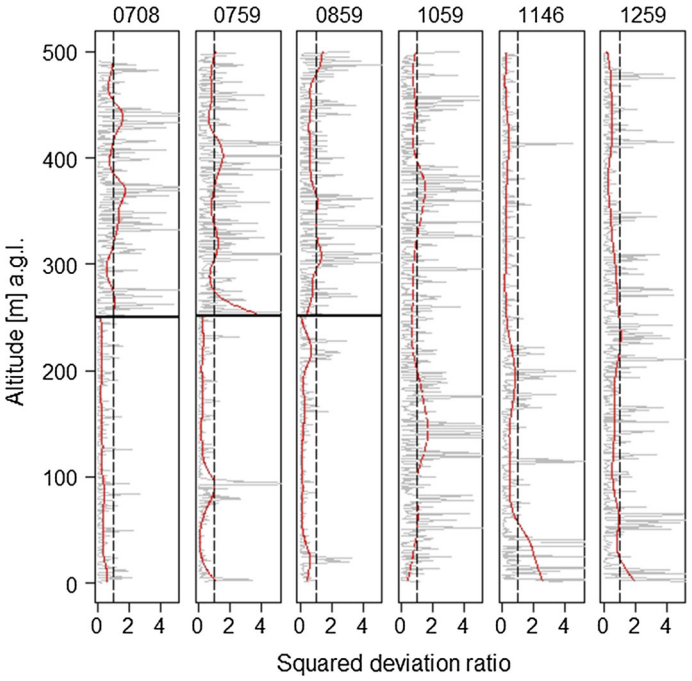

Fig. 8 *SDR* profiles of kriging estimates (grey lines) and smoothing splines (red lines). Dashed lines are the ideal ratio of 1

The degree of deviation from the theorized second-order scaling relationship inherent to the inertial subrange of turbulence was assessed through cross-validation of universal kriging. It was determined that during stable, early morning ABL conditions (with altitudes < 250 m a.g.l.), the process is less variable (i.e., less random) than the 2/3-power law model, which led to the *SDR* values to be less than 1 along the extent of these profiles. The subsequent three flights occurring later in the morning exhibited temperature scaling that was more consistent with the theorized 2/3-power law model. The theorized scaling was present along most of the profile from Flight 4 and on Fights 5–6 at altitudes from roughly 50–200 m a.g.l.

5 Discussion

While turbulence in the inertial subrange is considered to be isotropic and spatially stationary (i.e., homogenous), the vertical profiles of temperature from which turbulent fluctuations can be inferred are not spatially stationary. Thus, they require a modified form of the structure function to account for the non-constant mean across the spatial domain. Geostatistical approaches are well-suited for modelling random variables experiencing non-stationarity. In this study, we aimed to characterize the vertical structure of temperature profiles captured via WxUAS using geostatistical tools and more specifically: (1) use the variogram to identify sample separation distances that are inherent to the inertial subrange of turbulence, (2) assess the degree of deviation from the theoretical 2/3-power law scaling relationship, and (3) distinguish specific altitudes for which the scaling relationship can be resolved through universal

kriging estimates of the temperature profiles using weights assigned by the 2/3-power model variogram.

5.1 Resolution of Theorized Scaling and Model Fit

In pursuit of these objectives, we found that after detrending the data to account for the non-stationary mean, the fitted 2/3-power law model variograms were generally successful in modelling the spatially autocorrelated error components of the random variable (temperature), particularly in well-mixed conditions, thereby allowing us to identify sample separation distances that were inherent to the inertial subrange of turbulence. An analysis of the behaviour of the spatial autocorrelation can lead to a better understanding of the relationship between the power-law scaling parameter and the process being modelled.

Power-law model variograms (Eq. 14) are valid when the scaling exponent is $0 > \alpha > 2$; when $\alpha = 1$, the variogram is linear, and successive increments are stationary and independent. The limits of α, 0 and 2, represent a constant variance for all h and differentiable, non-random variation, respectively. As α approaches 2, the variogram becomes increasingly parabolic, whereas $\alpha \approx 0$ is indicative of a white-noise process (Webster and Oliver 2007). A more thorough understanding of the autocorrelation may be achieved through what Mandelbrot and Van Ness (1968) describe as fractional Brownian motions. In fractional Brownian motions successive increments are autocorrelated. When $\alpha > 1$, the increments are positively correlated, meaning they tend to move in the same direction. Conversely, when $\alpha < 1$, the error increments are negatively correlated, meaning they tend to move in opposite directions (Webster and Oliver 2007). Few processes in nature are represented by a power law with $\alpha < 1$, but turbulence is a notable exception. The negative spatial autocorrelation inherent to inertial subrange turbulence makes its spatial prediction challenging.

Flight 1a, below 250 m a.g.l., displays temperature scaling that follows the 2/3-power law model. The variogram of the subsequent Flight 2a estimated from data below 250 m a.g.l. is more parabolic in nature, and beyond 60-m separation distances, measured temperature values become increasingly similar. Such behaviour in the measured autocorrelation is indicative of a periodic or oscillatory process. Indeed, parabolic behaviour of the variogram is often seen in physical processes influenced by gravity (Chiles and Delfiner 2012). Gravity waves are often present in a weakly-turbulent stable boundary layer (Stull 1988), and high wind shear is known to induce Kelvin–Helmholtz waves. This phenomenon was observed by Higgins et al. (2018) using distributed temperature sensing to profile the stable boundary layer using an sUAS. The precise cause of the periodic behaviour in the vertical variogram cannot be fully characterized here in and is thus an opportunity for further research.

Periodicity was not observed in the subsequent variogram of Flight 3 at 0859 LT, and C_2 was estimated to be roughly an order of magnitude less than the previous flight; C_2 estimated from Flight 4 was similarly low. The 1001 LT radiosonde wind-speed profile captured in the time between Flights 3–4 suggests the presence of geostrophic wind speeds with in excess of 15 m s^{-1} at approximately 900 m a.g.l. (Fig. 3). Van den Kroonenberg et al. (2012) attributed higher C_2 estimates aloft to the presence of a low-level jet. In contrast, we observed lower C_2 estimates from the two WxUAS profiles bounding the observed low-level jet.

The 2/3-power law model fit the variograms estimated from the data of Flights 4–6, indicating fully-developed isotropic turbulence in the ABL. The C_2 estimate increased by roughly an order of magnitude between Flights 4–5, then decreased slightly by Flight 6 at 1259 LT. Typically C_2 increases until approximately midday and then begins to decrease (Van den Kroonenberg et al. 2012). Our C_2 estimates from the final three flights behaved in

accordance with this assumption. A nugget variance, C_0, was fit to the final three flights as well. The more turbulent nature of the profile, as indicted by the variogram closely following the α value of 2/3, likely leads to greater discontinuity at the variogram's origin. Recall that α values less than 1 are representative of a process whose successive increments are negatively autocorrelated (i.e. more dissimilar). This roughness of the data likely contributed to the presence of the nugget variance.

5.2 Profile Estimation Using Universal Kriging

An SDR estimate of less than 1 indicates that the squared residual is less than the estimated kriging variance, and is an indication that the process being modelled is less variable than predicted. Kriging has the effect of smoothing the data, thus *SDR* estimates (and *MSDR* estimates) are expected to be below 1 even if the model is well fit to the data. Nevertheless, the *SDR* estimates are below 1 for nearly the full extent of profiles from Flights 1a, 2a, and 3a, meaning that the process is less variable (i.e. less random) than the 2/3-power law model. The *SDR* estimates from Flights 1b, 2b, and 3b are more variable than the model (values greater than 1). This suggests that estimation of the variogram from vertical profiles is sensitive to both the maximum separation distances for which it is estimated, as well as the vertical domain. The upper limit of the boundary layer is not well defined under stable conditions (Stull 1988), and entrainment processes have influence on the spatial autocorrelation of the temperature measurements therein. The *SDR* estimates from the final three flights were more successful in identifying portions of the profile when theorized temperature scaling was valid due to the turbulence being more well developed.

6 Conclusions

Variograms were estimated from vertical temperature profiles collected throughout the morning boundary-layer transition across two days in the San Luis Valley, Colorado. To account for the variation in temperature with altitude, a mean function was specified and the variogram was estimated from the residuals. Power-law model variograms with a 2/3 scaling exponent were fit to the sample variograms to assess the separation distances commensurate with the inertial range of turbulence and correspondingly, estimate the temperature structure parameter, C_2. We found that geostatistical methods for spatially non-stationary random variables were well suited to describe the vertical structure of temperature in the ABL. The variogram estimated from the residuals allowed for the resolution of the inertial subrange of turbulence. Local variance estimates obtained through cross-validation of universal kriging estimates allowed for identification of portions of the temperature profiles that conform to the theorized inertial subrange temperature scaling relationship. It was found that this relationship was not well resolved under stable conditions. Results are likely sensitive to maximum separation distances and the extent for which the variogram is estimated.

Acknowledgements This research is supported by a grant from the U.S. National Science Foundation (NSF) [IIA-1539070] "RII Track-2 FEC: Unmanned Aircraft Systems for Atmospheric Physics". The authors would like to thank the students and staff of the Unmanned Systems Research Institute (USRI) at Oklahoma State University for their help in data collection, particularly Racine Swick and Victoria Natalie. The authors would also like to thank Gijs de Boer for coordinating the LAPSE-RATE field campaign during summer 2018 and our colleagues at The University of Oklahoma's Center for Autonomous Sensing and Sampling for the surface and radiosonde data. The authors are also thankful for the helpful comments from the two anonymous reviewers.

References

Antonia RA, Hopfinger EJ, Gagne Y, Anselmet F (1984) Temperature structure functions in turbulent shear flows. Phys Rev A 30(5):2704

Avery AS, Whyte S, Brenner J, Natalie VA, Jacob JD (2019) Experimental measurement of flow field around a rotary wing unmanned aircraft for evaluation of onboard anemometer placement. In: 72nd Annual meeting of the APS division of fluid dynamics

Barbieri L, Kral ST, Bailey SCC, Frazier AE, Jacob JD, Reuder J, Brus D, Chilson PB, Crick C, Detweiler C, Doddi A, Elston J, Foroutan H, González-Rocha J, Greene BR, Guzman MI, Houston AL, Islam A, Kemppinen O, Lawrence D, Pillar-Little EA, Ross SD, Sama MP, Schmale DG, Schuyler TJ, Shankar A, Smith SW, Waugh S, Dixon C, Borenstein S, de Boer G (2019) Intercomparison of small unmanned aircraft system (sUAS) measurements for atmospheric science during the LAPSE-RATE Campaign. Sensors 19(9):2179

Bonin TA, Goines DC, Scott AK, Wainwright CE, Gibbs JA, Chilson PB (2015) Measurements of the temperature structure-function parameters with a small unmanned aerial system compared with a sodar. Boundary-Layer Meteorol 155(3):417–434

Braam M, Beyrich F, Bange J, Platis A, Martin S, Maronga B, Moene AF (2016) On the discrepancy in simultaneous observations of the structure parameter of temperature using scintillometers and unmanned aircraft. Boundary-Layer Meteorol 158(2):257–283

Brock FV, Richardson SJ (2001) Meteorological measurement systems. Oxford, New York

Calmer R, Roberts GC, Preissler J, Sanchez KJ, Derrien S, O'Dowd C (2018) Vertical wind velocity measurements using a five-hole probe with remotely piloted aircraft to study aerosol–cloud interactions. Atmos Meas Tech 11(5):2583–2599

Chiles J-P, Delfiner P (2012) Geostatistics: modeling spatial uncertainty. Wiley, New York

Cioni S, Ciliberto S, Sommeria J (1995) Temperature structure functions in turbulent convection at low Prandtl number. EPL 32(5):413–418

Cressie N (1990) The origins of kriging. Math Geol 22(3):239–252

Cressie N (1993) Statistics for spatial data. Wiley, New York

Donnell GW, Feight JA, Lannan N, Jacob JD (2018) Wind characterization using onboard IMU of sUAS, AIAA Aviation

Gawedzki K, Kupiainen A (1995) Anomalous scaling of the passive scalar. Phys Rev Lett 75:3834–3837

Grossmann S, Lohse D (1994) Scale resolved intermittency in turbulence. Phys Fluids 6(2):611–617

Harrison RG (2015) Meteorological measurements and instrumentation. Wiley, New York

Higgins CW, Wing MG, Kelley J, Sayde C, Burnett J, Holmes HA (2018) A high resolution measurement of the morning ABL transition using distributed temperature sensing and an unmanned aircraft system. Environ Fluid Mech 18(3):683–693

Jacob J, Chilson P, Houston A, Smith S (2018) Considerations for atmospheric measurements with small unmanned aircraft systems. Atmosphere 9(7):252

Koch SE, Fengler M, Chilson PB, Elmore KL, Argrow B, Andra DL Jr, Lindley T (2018) On the use of unmanned aircraft for sampling mesoscale phenomena in the preconvective boundary layer. J Atmos Ocean Technol 35(11):2265–2288

Kolmogorov AN (1941a) Local structure of turbulence in an incompressible fluid for very large Reynolds numbers. Dokl Akad Nauk SSSR 30:299–303

Kolmogorov AN (1941b) Interpolation and extrapolation of stationary sequences. Izvestiya the Academy of Sciences of the USSR. Ser Math 5:3–14

Konrad T, Hill M, Rowland R, Meyer J (1970) A small, radio-controlled aircraft as a platform for meteorological sensors. Johns Hopkins APL Tech Dig 10:11–19

Lee TR, Buban M, Dumas E, Baker CB (2017) A new technique to estimate sensible heat fluxes around micrometeorological towers using small unmanned aircraft systems. J Atmos Ocean Technol 34(9):2103–2112

Mandelbrot BB, Van Ness JW (1968) Fractional Brownian motions, fractional noises and applications. SIAM Rev 10(4):422–437

Marusic I, Heuer WD (2007) Reynolds number invariance of the structure inclination angle in wall turbulence. Phys Rev Lett 99(11):114504

Matheron G (1963) Principles of geostatistics. Econ Geol 58:1246–1266

Mathieu J, Scott J (2000) An introduction to turbulent flow. Cambridge University Press, Cambridge

Monin AS, Yaglom AM (1975) Statistical fluid mechanics. MIT Press, Cambridge

Myers D (1989) To be or not to be… stationary? That is the question. Math Geol 21(3):347–362

Obukhov AM (1949) Structure of the temperature field in turbulent flow. Geogr i Goofiz 2(1):58–69

Pebesma EJ (2004) Multivariable geostatistics in S: the gstat package. Comput Geosci 30(7):683–691

Platis A, Altstädter B, Wehner B, Wildmann N, Lampert A, Hermann M, Birmili W, Bange J (2016) An observational case study on the influence of atmospheric boundary-layer dynamics on new particle formation. Boundary-Layer Meteorol 158(1):67–92

Platis A, Moene AF, Villagrasa DM, Beyrich F, Tupman D, Bange J (2017) Observations of the temperature and humidity structure parameter over heterogeneous terrain by airborne measurements during the LITFASS-2003 Campaign. Boundary-Layer Meteorol 165(3):447–473

Schotanus P, Nieuwstadt FTM, De Bruin HAR (1983) Temperature measurement with a sonic anemometer and its application to heat and moisture fluxes. Boundary-Layer Meteorol 26(1):81–93

Smith M (2011) Warnings: the true story of how science tamed the weather. Greenleaf Press, Austin

Sreenivasan KR, Antonia RA (1997) The phenomenology of small-scale turbulence. Annu Rev Fluid Mech 29(1):435–472

Stull RB (1988) An introduction to boundary layer meteorology. Kluwer Academic Publishers, Dordrecht

Taylor GI (1938) The spectrum of turbulence. Proc R Soc London Ser A 164:476–490

van den Kroonenberg AC, Martin S, Beyrich F, Bange J (2012) Spatially-averaged temperature structure parameter over a heterogeneous surface measured by an unmanned aerial vehicle. Boundary-Layer Meteorol 142(1):55–77

Vindel JM, Yagüe C, Redondo JM (2008) Structure function analysis and intermittency in the atmospheric boundary layer. Nonlin Process Geophysis 15(6):915–929

Wainwright CE, Bonin TA, Chilson PB, Gibbs JA, Fedorovich E, Palmer RD (2015) Methods for evaluating the temperature structure-function parameter using unmanned aerial systems and large-eddy simulation. Boundary-Layer Meteorol 155(2):189–208

Webster R, Oliver MA (2007) Geostatistics for environmental scientists. Wiley, New York